

Supporting Information

Macroscale and nanoscale photoelectrochemical behavior of p-type Si(111) covered by a single layer of graphene or hexagonal boron nitride

Annelise C. Thompson, Burton H. Simpson, and Nathan S. Lewis*

Division of Chemistry and Chemical Engineering, California Institute of Technology, Pasadena, CA, 91125, United States

*Corresponding author: nslewis@caltech.edu

Table of Contents

• X-ray photoelectron spectra of p-SiO _x , p-Si/Gr, and p-Si/h-BN electrodes	S2
• Ultraviolet photoelectron spectra of p-Si-H, p-Si/Gr and p-Si/h-BN electrodes	S4
• Raman maps for typical Gr and h-BN samples	S5
• UV/Vis spectra for typical Gr and h-BN samples	S7
• Cyclic voltammetry of macroscale p-SiO _x electrodes	S8
• Additional fits for macroscale p-Si/Gr V _{oc} data	S9
• SECCM line scans on Gr and h-BN	S10
• Effective redox potential	S11
• Redox couple compatibility with nanoscale junctions	S12

Supporting Data

X-ray photoelectron spectra of p-SiO_x, p-Si/Gr, and p-Si/h-BN electrodes

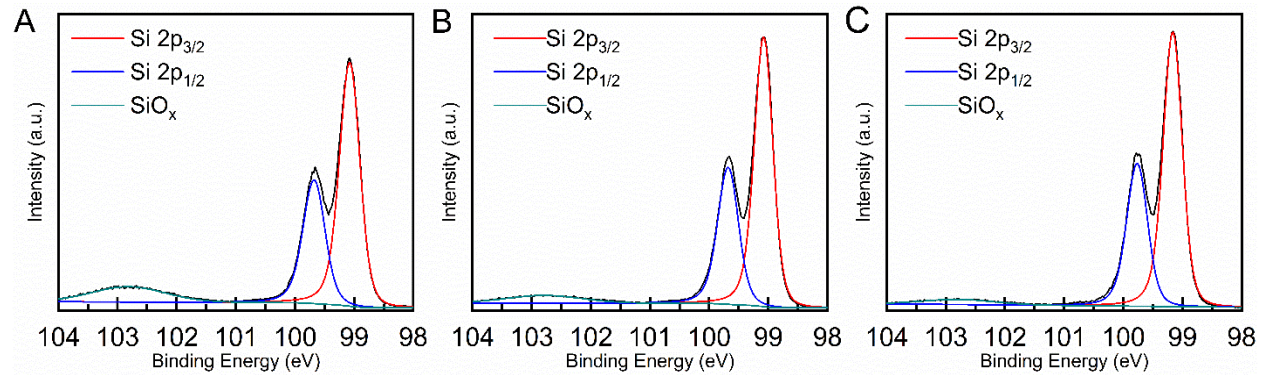


Figure S1. X-ray photoelectron spectra of p-Si surfaces. (A) The Si 2p region of a p-SiO_x electrode after fabrication. (B) The Si 2p region of a p-Si/Gr electrode after fabrication. (C) The Si 2p region of a p-Si/h-BN electrode after fabrication. The peaks at 99.2 and 99.8 eV are assigned to the Si 2p_{1/2} and 2p_{3/2} peaks, respectively, whereas the small peak at 102.5 eV is attributable to the oxide formed during the fabrication process.

The oxide introduced to the surface through the fabrication process was quantified using a simple substrate-overlayer model:

$$d = \lambda_{ov} \sin \theta \left[\ln \left(1 + \frac{I_{Si}^o}{I_{ov}^o} * \frac{I_{ov}}{I_{Si}} \right) \right]$$

where λ_{ov} is the attenuation factor through the oxide overlayer (2.6 nm),¹ θ is the angle from the surface to the detector, I_{Si}^o/I_{ov}^o is the instrument normalization factor expected from uncontaminated Si and SiO₂ samples, which was taken as 1.3 for this instrument, I_{ov} is the measured intensity of the silicon oxide peak found around 103 eV, and I_{Si} is the measured intensity of the silicon. Using this equation, an oxide of ~ 0.22 nm in thickness was detected on the p-Si/Gr electrodes and an oxide of ~ 0.22 nm in thickness was detected on the p-Si/h-BN electrodes. A monolayer of oxide is about 0.35 nm thick, so the average electrode with a 2D overlayer tested in this work had less than a monolayer (ML) of oxide growth after the

fabrication process. Substantially more oxide of ~ 0.50 nm in thickness was detected on the p-SiO_x electrodes, equivalent to 1.5 ML.

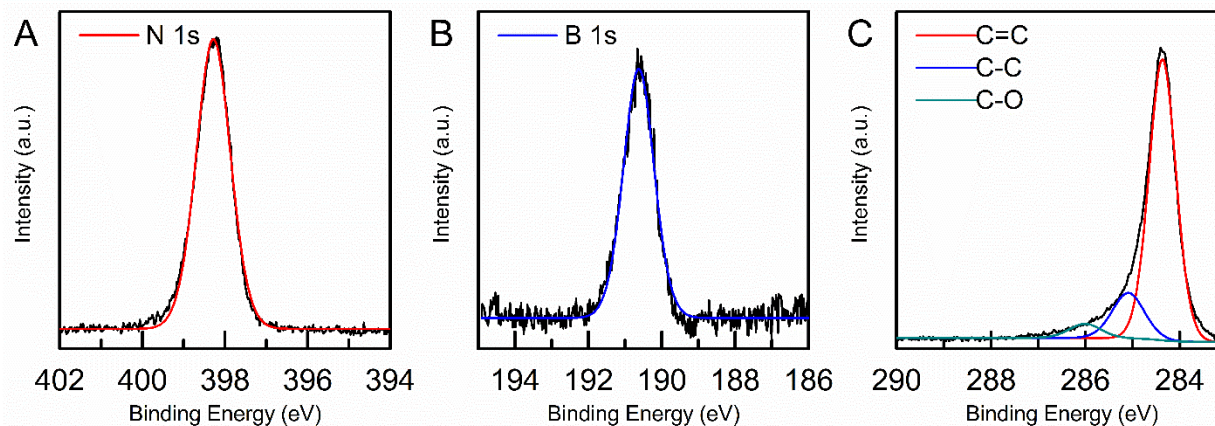


Figure S2. X-ray photoelectron spectra of A) the N 1s and B) the B 1s region of a typical h-BN sample and C) the C 1s region of a typical Gr sample.

Figure S2 shows the X-ray photoelectron spectra for typical p-Si/Gr and p-Si/h-BN samples after an anneal under forming gas. Figure 2a-b displays the N 1s and B 1s regions of a h-BN sample with single peaks at 398.3 eV and 190.6 eV respectively, yielding a 1:1 ratio of B:N from the peak area ratio, after adjusting for elemental relative sensitivity factors. The C 1s region of a p-Si/Gr sample in Figure 2c had three peaks at 284.4 eV, 285.0 eV, and 286.1 eV, ascribable to the sp² carbon bonds of graphene and the residual C-C and C-O bonds of the PMMA transfer support, respectively.

Ultraviolet photoelectron spectra of p-Si-H, p-Si/Gr and p-Si/h-BN electrodes

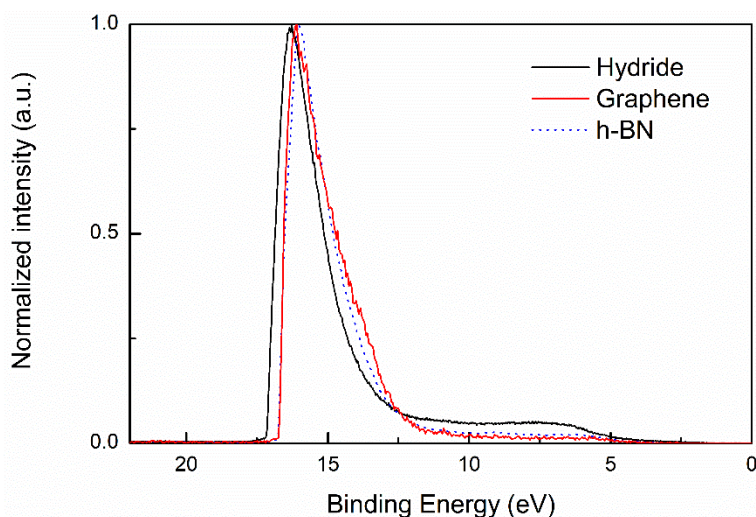


Figure S3. Ultraviolet photoelectron spectra of annealed p-Si-H, p-Si/Gr and p-Si/h-BN samples, corrected with reference to a sputter-cleaned Au sample.

The work function of each sample was calculated by extrapolating the slope of the secondary-electron cutoff to its intercept with the x-axis, and subtracting that value from the excitation energy of He I (21.21 eV). The data before and after annealing are shown in Table S1 and are the results of measurements on at least four samples. The magnitude of the work function for p-Si-H was different from the value calculated from the dopant density (5.02 eV) but is consistent with the band-bending and dipole expected on this surface². The work function and surface dipole of the p-SiO_x surface was the same as the p-Si/Gr and p-Si/h-BN surfaces, within error.

Table S1. Secondary electron cutoff, dipole, and work function of samples*

Sample	Before anneal				After anneal			
	SEC eV	$E_{\text{VBM}}^{\text{S}}$ eV	δ eV	W_{F}^{S} eV	SEC eV	$E_{\text{VBM}}^{\text{S}}$ eV	δ eV	W_{F}^{S} eV
p-Si-H	16.94	0.53(1)	-0.37(9)	4.27(10)	16.80	0.51(2)	-0.25(5)	4.40(7)
p-SiO _x	16.60	0.29(20)	-0.27(16)	4.60(6)	16.28	0.25(6)	+0.01(13)	4.92(17)
p-Si/Gr	16.51	0.40(3)	-0.07(2)	4.70(2)	16.47	0.58(6)	+0.14(5)	4.73(7)
p-Si/ h-BN	16.75	0.49(2)	-0.22(10)	4.45(9)	16.44	0.40(2)	0.00(8)	4.77(6)

*Standard deviations for $E_{\text{VBM}}^{\text{S}}$, δ , and W_{F}^{S} are shown in parentheses and are in units of hundredths of an eV (ceV).

Raman maps for typical Gr and h-BN samples

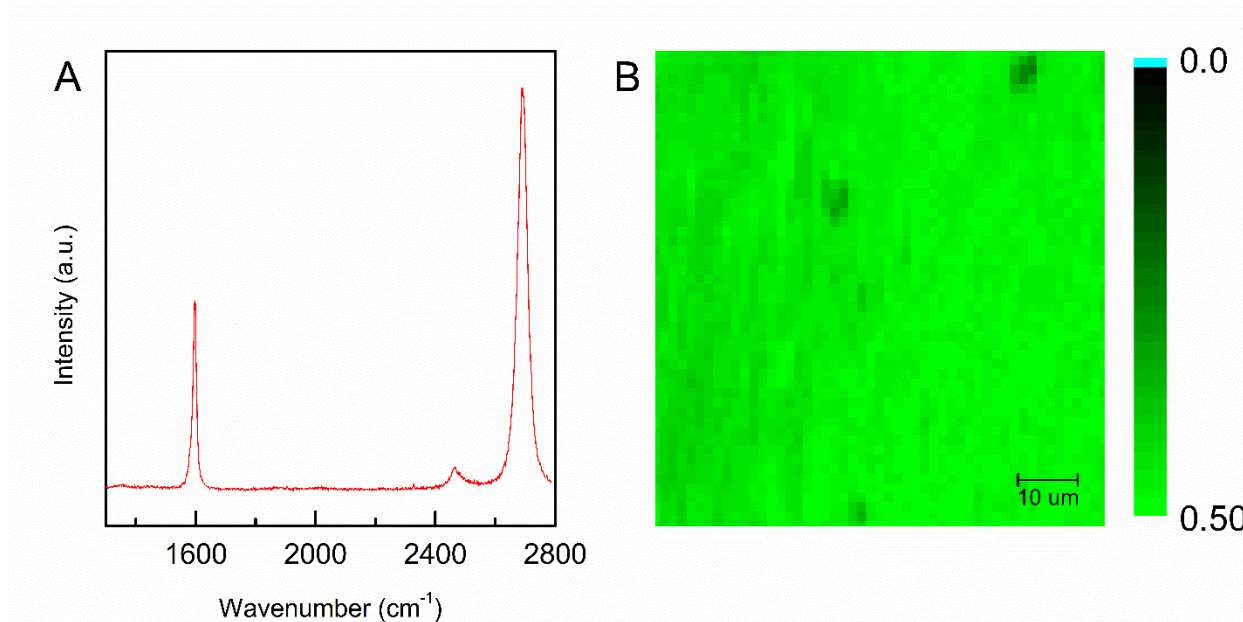


Figure S4. Raman spectra of a Gr sample on 300 nm thick SiO₂. (A) A typical Raman spectrum for a Gr sample. (B) Contour plot of I_G/I_{2D} for a typical monolayer Gr sample from a Raman map. The plot displays data for a 75x75 μm region on the sample.

Figure S4 shows both the typical Raman spectrum for a spot on a graphene sample and the contour plot of the intensity of the G peak to the intensity of the 2D peak (I_G/I_{2D}) ratio. The 95% of values observed for this ratio were between 0.4 and 0.5, indicating the presence of intact monolayer Gr.³ Some regions of lower intensity were observed, but the majority of the area was covered with pristine monolayer graphene.

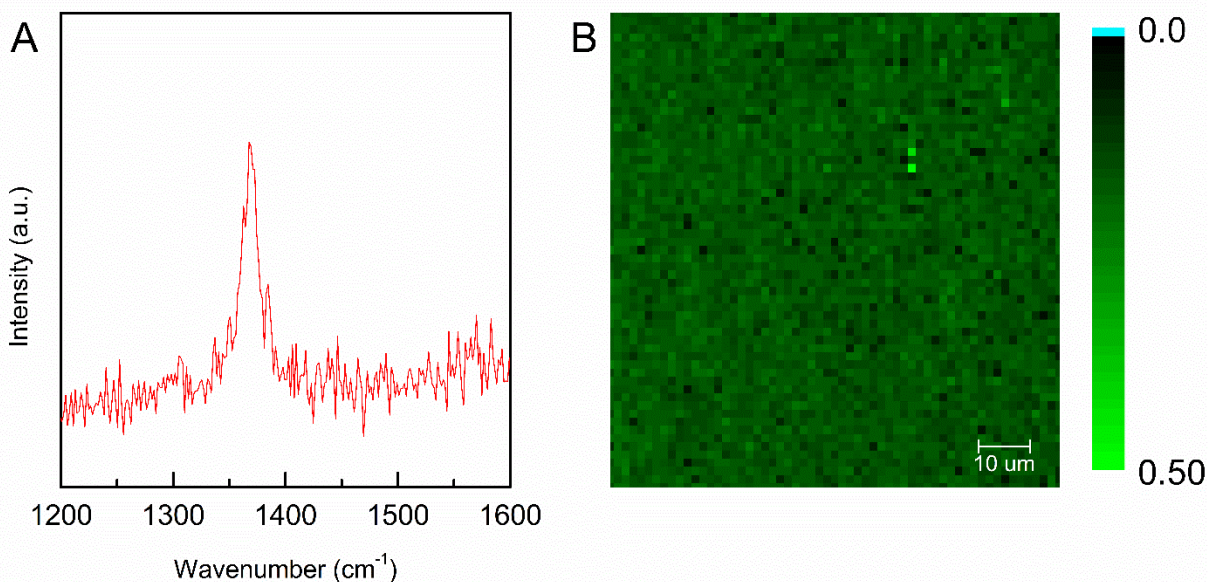


Figure S5. Raman spectra of an h-BN sample on 300 nm SiO₂. (A) A typical Raman spectrum for a h-BN sample. (B) Contour plot of the peak intensity for a typical monolayer h-BN sample from a Raman map. Although the intensity varied across the sample, the 1370 cm⁻¹ peak was present in each spectra. The plot displays data for a 75x75 μm region on the sample.

In Figure S5, the Raman spectrum of h-BN had a single peak at 1367 cm⁻¹ and thus the contour plot showed only the relative intensity of different spots on a sheet of h-BN.⁶ The intensity varied across the h-BN sheet, but no voids were visible at this scale. Each contour plot exceeded the size expected for a single grain of Gr or h-BN, given an average diameter of 50 μm and 5 μm, respectively. The scale for each plot was set so that regions with no intensity should be bright blue, to differentiate between regions of variable and no intensity.

UV/Vis spectra for typical Gr and h-BN samples

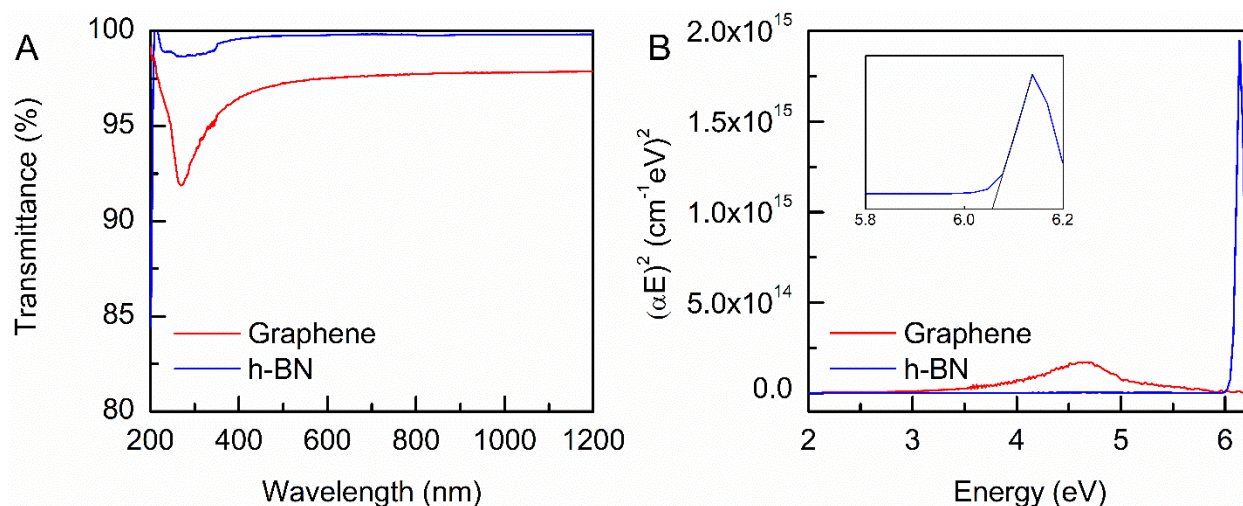


Figure S6. UV/Vis spectra for (A) Gr and h-BN samples on quartz slides and (B) Tauc plots for h-BN and Gr. The optical band gap of h-BN was determined to be 6.07 eV from extrapolation of the linear region of the Tauc plot to an intercept with the x-axis. The fit is shown in the inset. The same plot for the graphene showed no sharp increase that would indicate of the presence of a band gap.

Figure S6 displays the UV/vis spectra for Gr and h-BN on quartz. h-BN shows almost no absorption across the visible light region (400-700 nm) while Gr absorbs 2.7% of light in the same region. The optical band gap of h-BN was determined to be 6.07 eV from extrapolation of the linear region of the Tauc plot to an intercept with the x-axis, which is within the typical bounds for the polycrystalline material.⁸ The same plot for the graphene showed no such sharp increase that would indicate of the presence of a band gap.

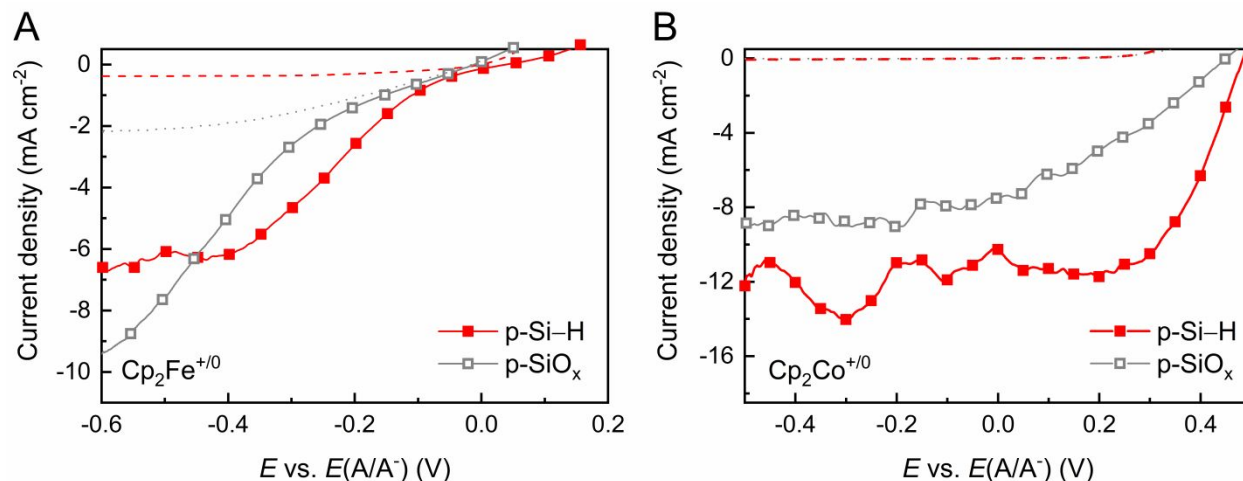


Figure S7. Photocurrent density vs potential (J - E) behavior of p-Si-H and p-SiO_x electrodes in contact with Cp₂Fe⁺⁰ (A) and Cp₂Co⁺⁰ (B), in CH₃CN-0.50 M LiClO₄ under 100 mW cm⁻² of ELH-type simulated solar illumination. The dashed lines show scans of the same electrodes without illumination.

Figure S7 presents the representative macroscale current density versus potential (J - E) behavior for p-Si-H and p-SiO_x electrodes in the dark and under illumination. The p-SiO_x electrodes exhibit similar behavior to the p-Si-H electrodes, although the magnitude of V_{oc} and the fill factor as lower for p-SiO_x.

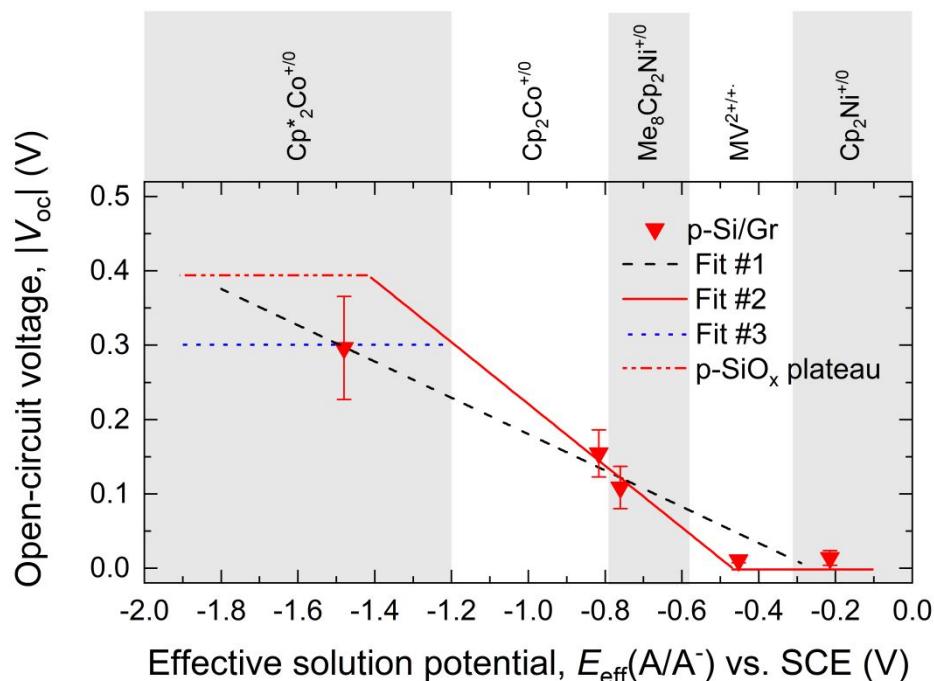


Figure S8. Possible linear fits for V_{oc} measurements on macroscale p-Si/Gr electrodes extrapolated to the plateau for the macroscale p-SiO_x electrodes, with the effective solution potential measured vs a saturated calomel electrode (SCE). Fit #1 is the linear fitting of the V_{oc} values in contact with CoCp*₂^{+/0}, CoCp₂^{+/0}, Me₈Cp₂Ni^{+/0}, and MV^{2+/+} with an R² of 0.970 and excludes NiCp₂. Fit #2 excludes Cp*₂Co^{+/0} as well as NiCp₂ and has a lower R² of 0.773, whereas Fit #3 shows where a plateau in V_{oc} could be, given the maximum V_{oc} value for p-Si/Gr electrodes as indicated by the measurements in contact with CoCp₂^{+/0}.

Three possible fits of the data are shown in Figure S8. Each fit is a linear fit and extrapolation of the data including direct weighting of the standard deviation. Fit #1 is the fit shown in the main text, with a slope of -0.24. Fit #1 and #2 are shown with a theoretical plateau at 400 mV, which is the plateau value of V_{oc} for p-SiO_x and p-Si/h-BN measured in this work, while Fit #3 takes into consideration that the plateau may be lower for p-Si/Gr. Fit #3 has a plateau at 300 mV, the mean value for p-Si/Gr in contact with Cp*₂Co^{+/0}. Given data for previous work modifying a Si surface with a monolayer of carbon atoms, each set of data here is expected to have a parallel slope, making Fit #2 (slope of -0.42) a viable fit when compared with the slopes from the other macroscale electrodes (slopes of -0.41-0.45, Table S2). Further macroscale measurements at more negative potentials would help to clarify the behavior of p-Si/Gr under these conditions. If the additional measurements gave credence to Fit#2, the differences between Gr and h-BN highlighted in the main text would still be giving rise to a much more negative onset in the slope of V_{oc} , a conclusion which is still corroborated by the nanoscale measurements performed in this work.

Table S2. Linear fit data for macroscale measurements from main text*

Sample	Slope	X-axis intercept (V)	R ²
p-Si-H	-0.414(33)	0.423(174)	0.969
p-SiO _x	-0.431(104)	0.073(12)	0.800
p-Si/Gr	-0.244(25)	-0.262(33)	0.970
p-Si/h-BN	-0.454(67)	-0.060(6)	0.919

*The error for slope is given in milli-units as slope is unitless. The error for the x-intercept is given in mV.

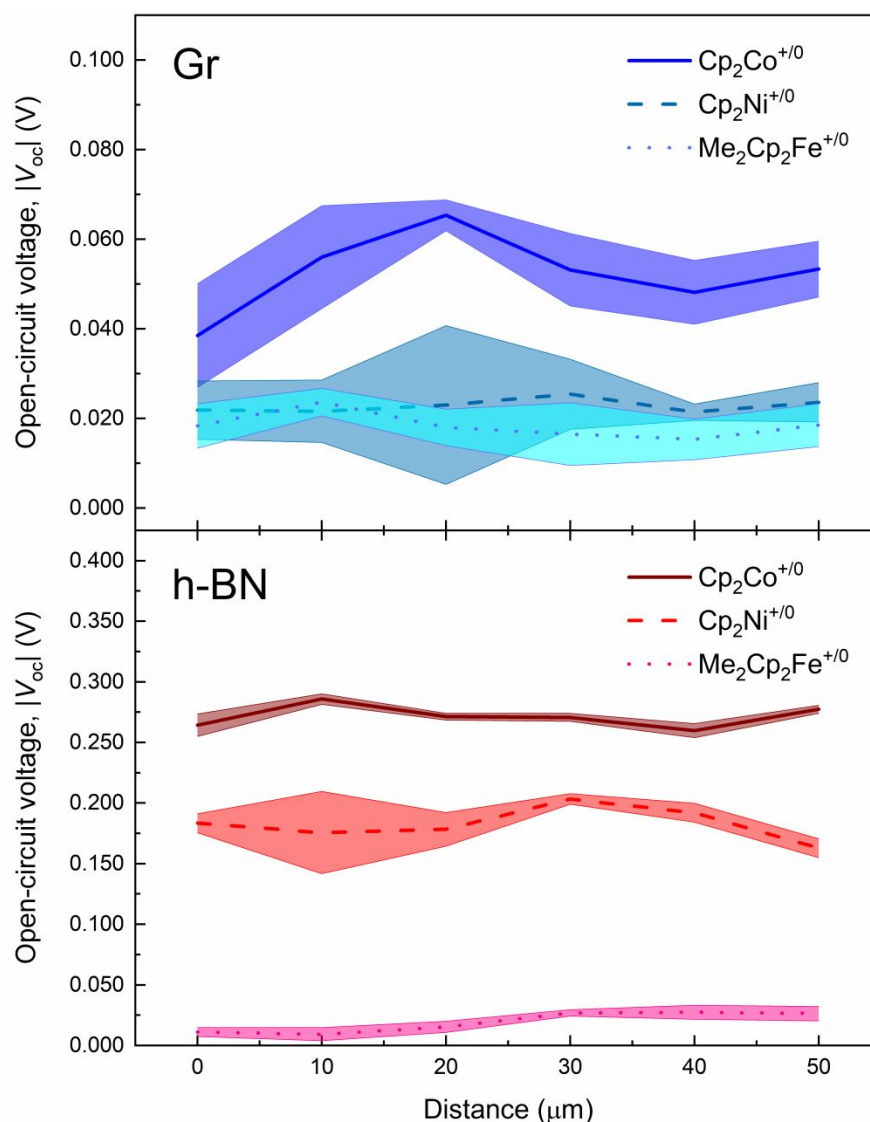


Figure S9. SECCM line scan of V_{oc} in 10 μm steps on Gr (upper) and h-BN (lower) in contact with $\text{Cp}_2\text{Co}^{+/0}$, $\text{Cp}_2\text{Ni}^{+/0}$, and $\text{Me}_2\text{Cp}_2\text{Fe}^{+/0}$, respectively. Each value is the average of six measurements at the same spot. Standard deviations are represented by the shaded regions surrounding each scan.

The measurements in Figure S9 were taken in consecutive 10 μm steps, although each scan with a different redox couple was collected on a separate region of the sample, to avoid cross contamination of the redox species. For p-Si/Gr, the measurements for $\text{Cp}_2\text{Ni}^{+/0}$ and $\text{Me}_2\text{Cp}_2\text{Fe}^{+/0}$ were very similar and showed little spatial variation across the measured region. The V_{oc} values for pSi/Gr in contact with $\text{Cp}_2\text{Co}^{+/0}$ were distinctly higher and showed a variation between steps of a magnitude consistent with expectations for line defects or grain boundaries (10-30 mV).⁴ The V_{oc} of the p-Si/h-BN sample in contact with the same redox couples shifted over a much wider range of potentials but exhibited a relatively low variation between steps. The measurements of V_{oc} in contact with $\text{Cp}_2\text{Ni}^{+/0}$ showed the largest standard deviations across the

surface on both the p-Si/Gr and p-Si/h-BN, consistent with expectations given the low solubility of this redox couple on the test electrolyte solution.

S1. Effective solution potential

As the solubility of the redox couples in this work were not identical, the concentrations used in each solution varied enough to affect the resulting measurements of V_{oc} . Grimm et. al. have previously explained a method by which the solution potential ($E(A/A^-)$) can be converted to the effective solution potential ($E_{eff}(A/A^-)$) to account for the differences in concentration of the minority acceptor, using a derivative of the Nernst equation. The full derivation and explanation for these shifts can be found in Ref. 31. The effective cell potential (E_{eff}) was calculated using the equation

$$E_{eff}(A/A^-) = E(A/A^-) - \frac{k_B T}{q} \ln \frac{[A_{eff}]}{[A]}$$

where $E(A/A^-)$ was the cell potential of the redox couple vs. SCE, $[A]$ was the minority acceptor concentration, and $[A_{eff}] = 10$ mM. Table 1 shows the concentrations actually used to make each solution, but the values for V_{oc} are normalized to $[A_{eff}] = 10$ mM.

S2. Redox couple compatibility with nanoscale junctions

Carrier transport accounts for much of the incongruity between macroscale and SECCM measurements, but SECCM presents unique experimental challenges when working with some specific redox couples. Measurements with $Cp^*_2Co^{+/0}$ and $Cp_2Ni^{+/0}$ were respectively impacted by issues associated with the reactivity and solubility of these compounds. Because of the extremely negative potential of the $Cp^*_2Co^{+/0}$ couple, $Cp^*_2Co^0$ can be oxidized to $Cp^*_2Co^+$ by reaction with oxygen. The need for a solvent saturated atmosphere to ensure stability of the liquid junction requires that the SECCM be operated in a flush box rather than a recirculating glove box, because the evaporated solvent would poison the catalyst used to remove water in a recirculating system. However, the flush box had a relatively higher oxygen content, resulting in faster conversion of $Cp^*_2Co^0$, and consequently producing a positive shift in E_{eff} for this couple during experiments. This shift was observed to occur so rapidly that only a few measurements could be taken before the solution potential was no longer well-defined by $Cp^*_2Co^{+/0}$. During bulk electrolysis of Cp_2Ni^0 , the Cp_2Ni^+ was observed to have very limited solubility (~ 1 mM) in the $LiClO_4$ solution. While enough Cp_2Ni^+ could be generated by bulk electrolysis to produce a stable E_{eff} , local Cp_2Ni^+ concentrations at the interface went above the solubility limit during cathodic operation. This insolubility would result in unstable interfaces and V_{oc} measurements during extended operation at a single point. These limitations can in principle be overcome by careful selection of redox couples, but the need for several facile redox couples across a wide range of potentials necessitated the use of these non-optimized redox species.

References

1. Hochella, M. F.; Carim, A. H., A reassessment of electron escape depths in silicon and thermally grown silicon dioxide thin films. *Surface Science* **1988**, *197* (3), L260-L268.
2. Gleason-Rohrer, D. C.; Brunschwig, B. S.; Lewis, N. S., Measurement of the Band Bending and Surface Dipole at Chemically Functionalized Si(111)/Vacuum Interfaces. *The Journal of Physical Chemistry C* **2013**, *117* (35), 18031-18042.
3. Ferrari, A. C., Raman spectroscopy of graphene and graphite: Disorder, electron-phonon coupling, doping and nonadiabatic effects. *Solid State Communications* **2007**, *143* (1–2), 47-57.

4. Long, F.; Yasaei, P.; Sanoj, R.; Yao, W.; Král, P.; Salehi-Khojin, A.; Shahbazian-Yassar, R., Characteristic Work Function Variations of Graphene Line Defects. *ACS Applied Materials & Interfaces* **2016**.